

AD-A145 368

CONTRIBUTIONS TO THE INTERNATIONAL ACOUSTIC EMISSION
SYMPOSIUM (7TH)(U) CALIFORNIA UNIV LOS ANGELES DEPT OF
MATERIALS SCIENCE AND ENG. H B TEOH ET AL. SEP 84

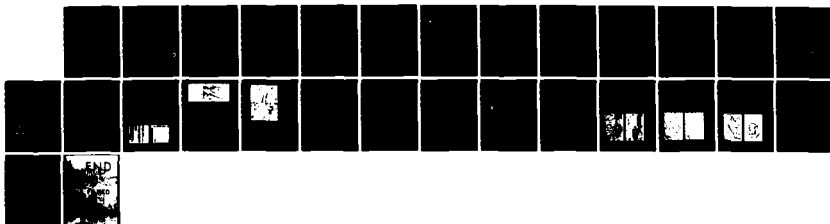
1/1

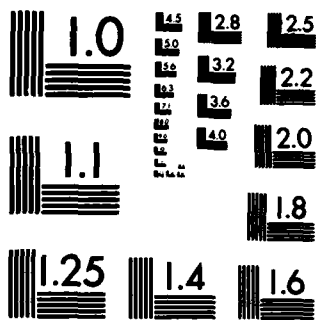
UNCLASSIFIED

TR-84-1 N00014-81-K-0011

F/G 20/1

NL





MICROCOPY RESOLUTION TEST CHART
NATIONAL BUREAU OF STANDARDS-1963-A

12

SECURITY CLASSIFICATION OF THIS PAGE (When Data Entered)

REPORT DOCUMENTATION PAGE		READ INSTRUCTIONS BEFORE COMPLETING FORM	
1. REPORT NUMBER 84-1	2. GOVT ACCESSION NO.	3. RECIPIENT'S CATALOG NUMBER	
4. TITLE (and Subtitle) Contributions to the 7th International Acoustic Emission Symposium		5. TYPE OF REPORT & PERIOD COVERED Technical	
		6. PERFORMING ORG REPORT NUMBER	
7. AUTHOR(s) H.B. Tech, I. Roman, M.M. Kwan M. Shibata and K. Ono		8. CONTRACT OR GRANT NUMBER(s) N00014-81-K-0011	
9. PERFORMING ORGANIZATION NAME AND ADDRESS Materials Science and Engineering Department 6532 Boelter Hall, University of California Los Angeles, CA 90024		10. PROGRAM ELEMENT, PROJECT, TASK AREA & WORK UNIT NUMBERS 61153N NR 384-700 RR011-08-01	
11. CONTROLLING OFFICE NAME AND ADDRESS Physics Division ONR-800 North Quincy St. Arlington, Virginia 22217		12. REPORT DATE September 1984	
		13. NUMBER OF PAGES 25	
14. MONITORING AGENCY NAME & ADDRESS (if different from Controlling Office)		15. SECURITY CLASS. (of this report) Unclassified	
		15a. DECLASSIFICATION DOWNGRADING SCHEDULE	
16. DISTRIBUTION STATEMENT (of this Report) Unlimited Reproduction in whole or in part is permitted for may purpose of the U.S. Government			
17. DISTRIBUTION STATEMENT (of the abstract entered in Block 20, if different from Report)			
18. SUPPLEMENTARY NOTES To be published in the Proceedings of the 7th International AE Symposium Zao, Japan, Oct. 84..			
19. KEY WORDS (Continue on reverse side if necessary and identify by block number) Acoustic Emission Fe-Ni alloys Heat Treatment Glass-fiber reinforced composite A533B Steel Magnetomechanical acoustic emission			
20. ABSTRACT (Continue on reverse side if necessary and identify by block number) This report is a collection of three preprints, of which abstracts appear on pages 1,9 and 17.			

AD-A145 368

DTIC FILE COPY

DTIC ELECTED
SEP 14 1984

DD FORM 1 JAN 73 1473

SECURITY CLASSIFICATION OF THIS PAGE (When Data Entered)

84 09 13 059

Contents: Magneto-mechanical Acoustic Emission-Temperature Effects; Acoustic Emission Characterization of Failure Mechanisms in Woven Roving Glass-Epoxy Composites; and Fracture Induced Acoustic Emission of A533B Steel - Effects of Test Temperature and Fracture Mechanisms.

Magnetomechanical Acoustic Emission - Temperature Effects

May M. Kwan*, K. Ono and M. Shibata**

Department of Materials Science and Engineering
School of Engineering and Applied Science
University of California, Los Angeles, CA 90024 USA
*Now at TRW, Redondo Beach, CA and **at Hata Giken, Tokyo.

ABSTRACT

MAE behavior of ferromagnetic materials was investigated as a function of test temperature. MAE intensity was zero slightly above the Curie temperature and its temperature-dependence above 300 K was correlated with temperature-induced changes in saturation magnetic induction and saturation magnetostriction. Low temperature behavior was quite different and was attributed to effects of microdomains. The origins of these observations are discussed in terms of mechanisms deduced from various experiments correlating magnetic and AE behavior in a number of ferromagnetic materials.

INTRODUCTION

In our previous studies /1,2/, magnetomechanical acoustic emission (MAE) has been shown to originate from two principal sources. One is due to domain boundary displacement and contributes to pre-saturation MAE (Type I). The other appears to arise from microdomains (Neel spikes) and produces post-saturation MAE (Type II). Since temperature affects various magnetic parameters, we have investigated temperature dependence of MAE behavior of Ni and two Fe-Ni alloys (36% and 47% Ni). Results are generally consistent with expected behavior of the two types of MAE signals.

EXPERIMENTAL PROCEDURES

Sheet samples were used with a magnetic yoke arrangement (Fig. 1). The arms of the yoke was extended into an insulated chamber so that a sample could be heated by an electrical heater or cooled by vaporized liquid nitrogen. The magnetic field at 60 Hz was applied parallel to the sample axis and a waveguide was used to isolate a sensor from the hot or cold zone. The sensor was AET MAC300 having a broad-band response in the range 100-400 kHz. Filter bandwidth was 30 to 2000 kHz. Other experimental details were basically identical to those reported elsewhere /1,2/.

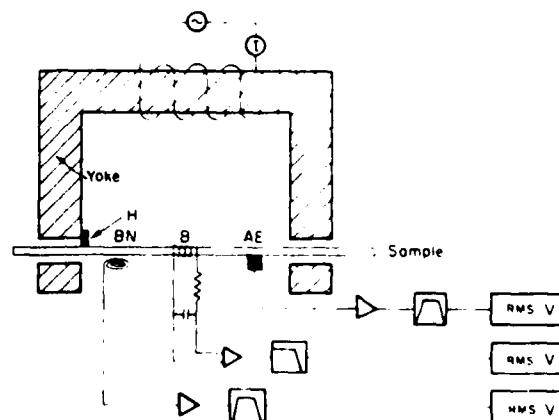


Fig. 1. Magnetic yoke arrangement for MAE and magnetic properties measurements.

RESULTS

a. Nickel

Magnetic field dependence of MAE intensities (rms voltage) of nickel at several temperatures are shown in Fig. 2. These experiments were conducted under isothermal conditions. MAE levels at weak fields were relatively unaffected by a lowering of test temperature, but saturation MAE levels were significantly increased at low temperatures. On the other hand, MAE levels both at weak fields and at saturation were decreased as temperature was elevated. As the field was increased further beyond the plateau region, MAE intensity exhibited another rise. Above the critical field, H^* , post-saturation MAE is initiated. H^* can be obtained by direct waveform observation. Temperature effect on H^* was small in the range -27° to 40°C , but H^* increased sharply between -27° and -95°C . Above 40°C , H^* decreased with increasing temperature. Temperature dependence of saturation MAE level and saturation magnetic induction of annealed nickel (800°C anneal) are shown in Fig. 3 for the temperature range from -120° to 358°C . Saturation MAE level and B_s have been normalized by their respective values at 25°C . The temperature scale is normalized by the Curie temperature, T_c . Below $0.6 T_c$ the rate of change of B_s with temperature was slow; however, MAE level rose steeply with decreasing temperature. Above $0.6 T_c$, the saturation magnetization level was lowered as temperature increased, approaching zero at T_c . Saturation MAE levels also decreased with temperature, but at a faster rate than B_s . The saturation MAE level diminished at slightly above T_c .

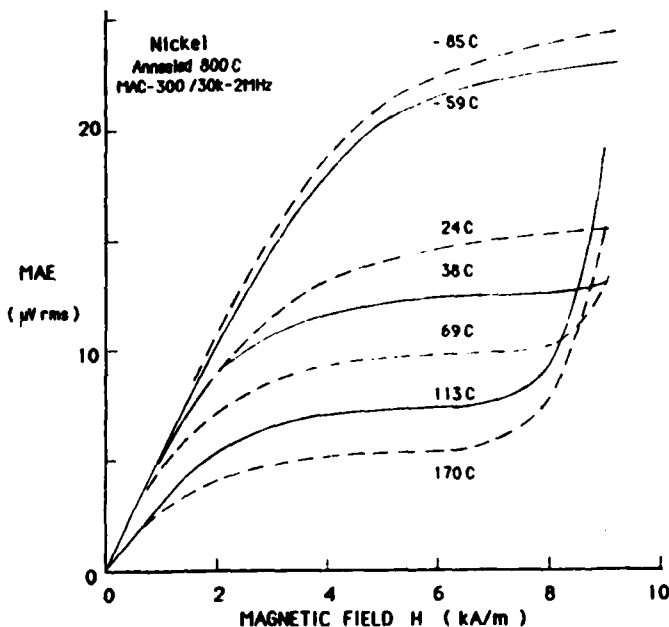


Fig. 2. Temperature and field dependence of MAE intensities for nickel, annealed at 800°C , 1/2 hr.

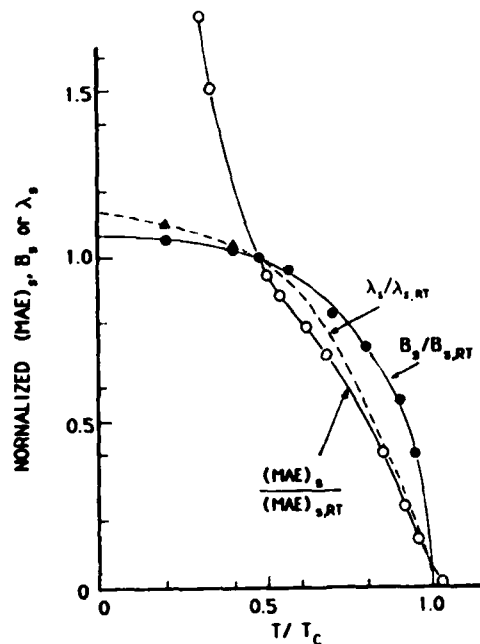


Fig. 3. Temperature dependence of saturation MAE level, λ , and B_s for annealed nickel (800°C , 1/2 hr).

b. Fe-Ni alloys

MAE signal intensities and saturation magnetic inductions of two annealed Fe-Ni alloys were measured as a function of field strength in the temperature range from 25° to 160°C . Typical curves of signal intensity as a function of applied field are shown for Fe-47%Ni in Fig. 4. The effect of increasing

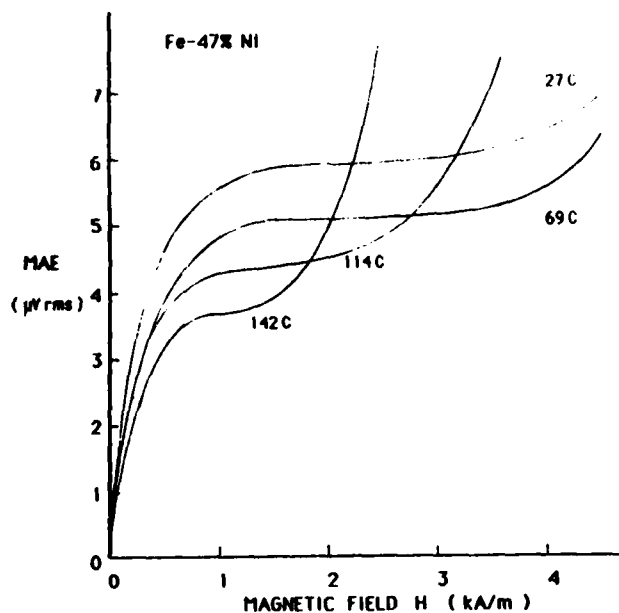


Fig. 4. Temperature and field dependence of MAE intensity for Fe-47%Ni.

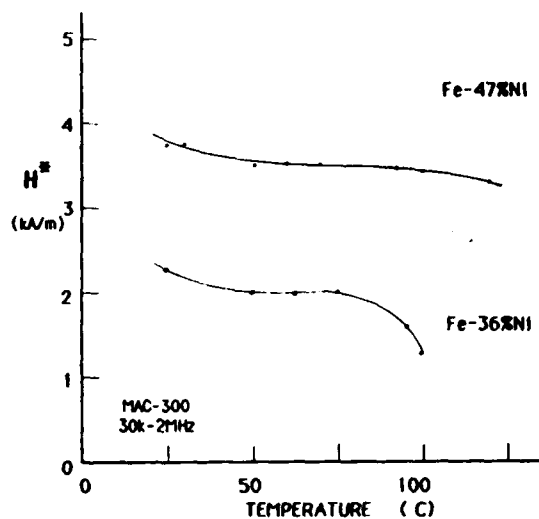


Fig. 5. H^* as a function of temperature for Fe-Ni alloys.

temperature was to reduce the overall MAE intensities at low fields up to the initial plateau in MAE level, and to decrease the saturation level. At 103°C (0.66 T), the level of MAE at saturation for Fe-36%Ni was approximately 60% of its value at 28°C. Similarly, the saturation level of MAE for Fe-47%Ni at 142°C was reduced to 63% of its value at 27°C (Fig. 4). Saturation magnetic induction was also decreased by increasing temperature; B_s at 103°C was decreased to 74% of its room temperature value for Fe-36%Ni. The rate of decrease in B_s with temperature was less rapid than that for MAE intensity. When Fe-36%Ni had undergone a 26% change in B_s at 0.66 T, its MAE level was reduced to 50% of its ambient temperature level. The effect was more pronounced in the Fe-47%Ni alloy for which a 7% temperature-induced change in B_s was accompanied by a 40% decrease in MAE intensity. Measured values of H^* are shown as a function of temperature for these two Fe-Ni alloys in Fig. 5. A strong temperature dependence of H^* for Fe-36%Ni was observed where H^* was reduced by 40% by elevating the temperature from 25° to 100°C.

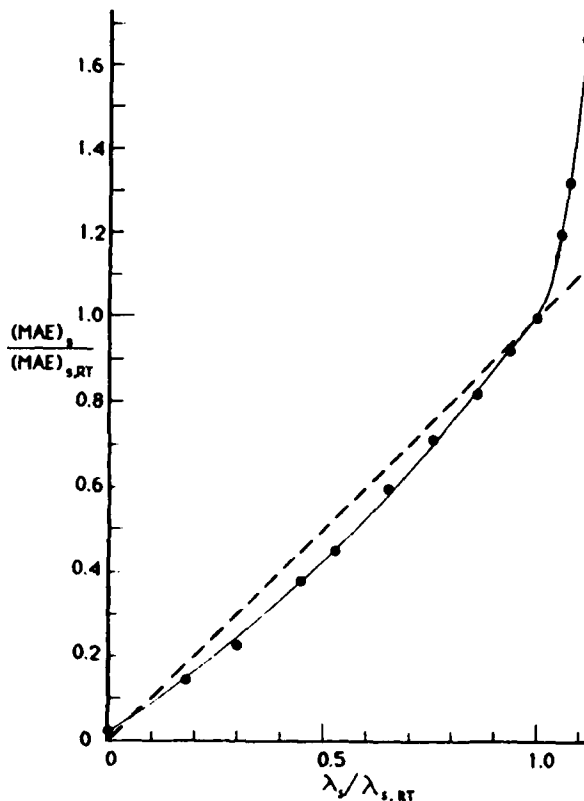
DISCUSSION

The temperature effects on two types of MAE will be considered. First, the temperature dependence of saturation MAE level will be examined. Following the discussions presented elsewhere, the intensity of MAE signals is expected to depend on temperature-induced change in magnetostriction, λ . The magnitude of the magnetostriction constants usually decreases with increasing temperature and approaches zero at T_c . Second, the influence of temperature on the appearance of the second MAE peak will be studied. Since this phenomenon takes place near the shoulder of the hysteresis loop, it is reasonable to expect that its behavior may reflect the temperature dependence of magnetocrystalline anisotropy energy. In cubic crystals, the temperature dependence of λ is generally not as strong as that for magnetocrystalline anisotropy. Magnetoelastic energy depends on the second-order terms of the direction cosines of magnetization vectors, whereas the anisotropy energy starts with fourth-order terms.

Accession For	
NTIS GRA&I	<input checked="" type="checkbox"/>
DTIC TAB	<input type="checkbox"/>
Unannounced	<input type="checkbox"/>
Justification	
By	
Distribution/	
Availability Codes	
Dist	Avail and/or Special
A-1	



Fig. 6. Saturation MAE level as a function of λ_s for nickel. These values are normalized by respective room temperature values.



a. Nickel

Saturation magnetostriction, λ_s , of polycrystalline Ni has been measured as a function of temperature by a number of investigators. In addition, theoretical calculations of magnetostrictive constants have been made by Vonsovsky /3/ who postulated a law of temperature dependence of magnetostriction which can be expressed as $\lambda_s = B_s^2$. The relationship holds well when the effects of spin-orbit interaction within the atoms are negligible. Measurements of λ_s for Ni made by Doring /4/ confirmed that this expression holds well for Ni. The decrease in the saturation MAE level, $(MAE)_s$, between room temperature and T_c can be correlated with the reduction in λ_s in this temperature range. $(MAE)_s$ and B_s and λ_s at a given temperature have been normalized by their respective room temperature values in Fig. 6. A proportionality can be established between $(MAE)_s$ and λ_s quantities for temperatures above $0.6 T_c$. However, the relationship between MAE levels and λ_s values falls short of the linear dependence as shown by a deviation from the dashed line in Fig. 6. Aside from a reduction in λ_s with increasing temperature, domain size is known to decrease at elevated temperatures /5/. Domain size, in turn, limits the volume swept out by each abrupt jump of a moving domain boundary, which is directly proportional to MAE intensity. Thus, a decrease in domain size at high temperatures contributes to the higher rate of decrease in MAE level than would otherwise be expected from the reduction in λ_s alone. The rapid increase in MAE level below T_c cannot be properly accounted for by a straight forward correlation with magnetostriction change. Recent experiment shows that high temperature annealing of nickel eliminates this low temperature increase in MAE level, suggesting that inclusions and grain boundaries play an important role as obstacles to domain boundary motion at low temperatures. Domain wall position and its movement in the presence of a magnetic field depend on the profile of the energy barrier existing in the material. In his theory of coercive force, Neel /6,7/ calculated this energy by considering the magnetic poles associated with

fluctuations in the direction of magnetization caused by variations in elastic stress and the fluctuations in intensity of magnetization associated with non-magnetic inclusions. In a material with large K_1 and small λ_s , the energy is associated with non-magnetic inclusions; on the other hand, a material with small K_1 and large λ_s , the energy is predominantly determined by fluctuations in strain. Due to the strong temperature dependence of K_1 in Ni, the above cases are applicable to describing the temperature dependence of its coercivity. When the influence of non-magnetic inclusions predominate, H_c is proportional to the quantity $(K_1/B_s)v''$, where v'' is the volume fraction of inclusions. When K_1 is small and λ_s is large, H_c is proportional to $(\lambda_s \sigma_i / B_s)v'$, where σ_i and v' are the magnitude of internal stresses and the volume fraction of material subjected to σ_i , respectively. Above ambient temperatures, K_1 is small for nickel and inclusions have negligible effect on H_c . As the magnitude of K_1 increases at low temperatures, the influence of inclusions on coercivity becomes increasingly important. At -100°C , K_1 exhibits a ten-fold increase over its value at 20°C . Inclusions can contribute to the observed low temperature increase in MAE level in two ways: (1) by interacting with domain wall motion and (2) by increasing the volume of 90° domains. Strong pinning of the moving domain boundaries causes pinned down segments to bow-out to a critical radius and eventually lead to its quick release from pinning points. The jump in domain wall occurs more abruptly, resulting in a decrease in the rise time over which the accompanying inelastic strain takes place. MAE intensity has been shown to vary inversely with rise time. Thus, strong pinning of domain walls by inclusions and grain boundaries can lead to an increase in MAE level. Secondly, as a consequence of the free magnetic poles on the surface of non-magnetic inclusions, they tend to create new 90° domain walls in order to minimize the overall magnetostatic energy. A linear relation has been found between coercivity and the volume of 90° domains in grain-oriented Fe-Si alloys /8/. Since the motion of 90° domain walls creates magnetostrictive strain change, the source of MAE, is increased by the presence of inclusions.

b. Fe-Ni alloys

Following the relationship between MAE and λ_s established for Ni, a similar correlation can be expected as a function of temperature in Fe-Ni alloys. The fractional changes in saturation MAE level and λ_s over their respective room temperature values indicates one-to-one relationship between these quantities. Although direct measurement of magnetostriction as a function of temperature is unavailable for Fe-Ni alloys, a decrease in λ_s with temperature can be expected from the reduction in B_s . For small changes in B_s ($B_s/B_{s,RT} > 0.80$), the room temperature relationship between λ_s and B_s was assumed in order to estimate the temperature-induced changes in magnetostriction based on the value of B_s at the particular temperature. When B_s changes are large ($B_s/B_{s,RT} < 0.80$), λ_s values cannot be approximated by the same B_s curve because the latter significantly deviate from the magnetically saturated condition and complicated assumptions become necessary concerning the distribution of various magnetization processes as a function of magnetization intensity. Moreover, it follows from the temperature dependence of K_1 that this distribution is expected to change with temperature even at a constant magnetization level.

The deviation exhibited by the experimental data arise from the combined effects of decreasing domain size and increasing contribution due to post-saturation magnetization processes at elevated temperatures. A comparison of the domain sizes in Fe-50%Ni at 10° , 235° , 250° and 300°C shows a tendency for domain refinement with increasing temperature /5/. Smaller domain size limits the volume swept for each domain wall jump, thereby reducing the source volume

of MAE signals. Secondly, K_1 values of Fe-36%Ni and Fe-47%Ni alloys are small and the saturation level of MAE must include a significant contribution from magnetization of small island domains. At high temperatures, anisotropy energy is further reduced so that even greater post-saturation contribution is expected.

It has been established that the field required to achieve nominal saturation is equal to the quantity $2 K_1/B_s$. Since T_c of Fe-36%Ni is 543°K, B_s is substantially reduced even at moderately high temperatures. Temperature effects on the theoretical saturation field strengths, $H(\text{sat})$, shows that $H(\text{sat})$ near 100°C is approximately half of that at 25°C. The minimum field strength necessary to observe a second peak in the MAE waveform is always larger than $H(\text{sat})$. This result suggests that the source of this Type II MAE operates only in well-saturated regions of the hysteresis loop where the change in magnetic induction with field strength is small, implying that the volumes being magnetized are small.

c. Temperature effect on post-saturation MAE

Since the magnitudes of the anisotropy constants, K_1 and K_2 , generally decrease with increasing temperature, we expect domain vector rotation and post-saturation magnetic processes to occur more readily at elevated temperatures. The saturation magnetic field level will also depend on the temperature dependence of magnetization vectors, M . A change in temperature not only alters the magnitude of K_1 , but can also change its sign. A sign change suggests a change in the relative order of easy, medium and hard axes of magnetization. For instance, the easy axes of pure nickel change from $\langle 111 \rangle$ at room temperature to $\langle 100 \rangle$ at temperatures above 200°C. Below room temperature, the easy axes lie along $\langle 111 \rangle$ directions, where anisotropy energy E_k is a minimum. The value of E_k becomes more negative as temperature is lowered, suggesting increasing stability of M along $\langle 111 \rangle$ directions. In other words, rotation of M out of the easy directions becomes more difficult at low temperatures. The minimum in E_k at $[111]$ is significantly reduced at 20°C and it is virtually eliminated at 150°C. This implies that magnetization rotation and macroscopic saturation can be attained at a lower driving force for magnetization at elevated temperatures. It follows that post-saturation magnetization processes can take place at lower applied fields. The field dependence of MAE intensities (Fig. 2) shows the second increase in MAE level at approximately 7 kA/m at 170°C and 8 kA/m at 38°C. Below 24°C, no such increase in MAE level was observed for field strengths less than 9 kA/m. These results are consistent with the decrease in E_k above 24°C and the increase in E_k below ambient temperatures. The critical field at which post-saturation MAE signals is initiated, H^c , is equivalent to a coercive force, H_c , acting to overcome the gradient of the total energy associated with obstacles to domain motion. According to Neel, the temperature dependence of coercive force in Ni can be separated into three regions of behavior. At low temperatures (below -50°C), effects of non-magnetic inclusion dominate the behavior of H_c whose magnitude is proportional to the quantity $(K_1/B_s)v''$ (Region I), where v'' is the volume fraction of inclusions. In the intermediate temperature range (-50° to +100°C), the contribution due to inclusions diminishes (Region II). The magnitude of K_1 remains substantial at these temperatures and fluctuations in internal strain become increasingly important in Region II. The latter's contribution to H_c is proportional to $(\lambda^2 \sigma_1^2 / K_1 B_s) v'$ where σ_1 and v' are the internal stresses and the volume fraction of material subjected to σ_1 , respectively. The combined effects of inclusions and internal stress influence the behavior of H_c at intermediate temperatures. The first of these decreases monotonically with temperature. The internal stress contribution, on the other hand, increases with temperature

within Region II. As K_1 become small above 50°C , temperature dependence of H_c is dominated by the influence of internal stresses since λ_s is large in Ni. Thus, in the high temperature range (Region III), H_c becomes proportional to $(\lambda_s \sigma_1 / B_s) v'$.

The observed temperature dependence for nickel annealed at 800°C implies the change in crystal anisotropy with temperature below -30°C (Region I). In the intermediate temperature range between -30° and $+30^\circ\text{C}$ where a three-fold decrease in K_1 values occurs, H^* was almost independent of temperature. This corresponds to the behavior within Region II, where the effects of impurities and internal stresses on H^* are additive. Above 50°C , the magnitude of K_1 is very small but H^* decreases with temperature as the effects of internal stress govern the temperature dependence of H^* (Region III). The role of impurities on the low temperature behavior of H^* was verified by comparing the temperature dependence of H^* for Ni annealed at 800°C for 1 hour and 1300°C for 3 hours. The main change between these two materials is grain size. Grain boundaries are apparently acting like inclusions or impurities in producing microdomains or island domains. While this interpretation needs to be supported further, the basic interpretation of MAE as related to H^* is consistent with Neel's theory.

The temperature dependence data of K_1 for Invar alloys (Fe-36%Ni) from various published sources shows considerable disagreement /9-11/. It has been suggested that K_1 for this alloy may be strongly influenced by impurity content, composition and thermal treatment. The anisotropy energy, E_k , of this alloy is essentially independent of the value of K_1 . K_1 for Fe-47%Ni is not strongly temperature sensitive in the range 0° to 140°C , but K_2 is strongly affected by temperature /11/. The easy axis of magnetization for this alloy is [100]; but [011], rather than [111], is the hard axis. Consequently, higher order terms involving K_2 must be included in evaluating the E_k profile. The reduction in the magnitude of K_1 with temperature in both Fe-Ni alloys is expected to promote easier rotation of the magnetization vectors and decrease the field strength for macroscopic saturation. However, the value of K_1 is too small, even at ambient temperatures, to expect it to influence the coercive force of these alloys. As a consequence of their relatively high λ_s values, internal stresses are more likely to interact with domain walls. The observed temperature dependence of H^* for Fe-36%Ni (Fig. 5) corresponds to the predicted behavior of coercive force within Regions II and III, where internal stress effects dominate. The nearly constant value of H^* for Fe-47%Ni suggests the behavior expected within Region II. In comparing the temperature effects on H^* for Fe-36%Ni and Fe-47%Ni, the former tends to indicate greater temperature dependence above 75°C . This result is a consequence of the lower Curie point of Fe-36%Ni ($T_c = 270^\circ\text{C}$). The magnitude of K_1 of this alloy approaches zero at 127° . H^* follows the characteristic behavior of Region III where the effects of internal stress dominate. The higher Curie point of Fe-47%Ni ($T_c = 540^\circ\text{C}$) and the slower rate of decrease of K_1 with temperature tend to widen the temperature range in which Region II behavior is exhibited. Thus, the value of H^* for Fe-47%Ni displayed only a 9% change over the temperature range 25° to 100°C .

CONCLUSIONS

1. Saturation MAE level of Ni and Fe-Ni alloys decreased with increasing temperature. The observed changes in MAE (of Type I) intensity closely followed the variation in saturation magnetostriction. This observation is consistent with our interpretation of Type I MAE; i.e., the motion of 90° domain walls.

2. Magnetic field levels (H^*), above which post-saturation (Type II) MAE is observed, decreased with increasing temperature. The origin of Type II MAE is suggested to be due to the elimination of small domains associated with various obstacles. Type II MAE behavior parallels that of coercive forces which has been rationalized by Neel theory using the concept of Neel spikes (or microdomains).
3. Grain size of Ni samples affected both Type I (saturation MAE level) and Type II (H^*) MAE behavior. These parameters increased substantially as test temperature was lowered below room temperature ($\sim T/2$) in fine-grained samples, whereas these remained constant in coarse-grained samples. The increases observed at low temperatures appear to arise from microdomains at grain boundaries. These produce pinning and unpinning of domain boundaries, increasing Type I MAE. Their own motion, rotation and disappearance contribute to Type II MAE.

ACKNOWLEDGEMENTS

This work was supported by the Office of Naval Research, Physics Program.

REFERENCES

1. May M. Kwan, Ph.D. Thesis, University of California, Los Angeles, 1983.
2. May M. Kwan, K. Ono and M. Shibata, to be published.
3. S. V. Vonsovsky, "Temperature dependence of magnetic anisotropy of Co single crystals," J. Phys. Moscow 3, 181-90, (1940).
4. W. Doring, "On the temperature dependence of magnetostriction of nickel," Z. Phys. 103, 560-82 (1936).
5. J. Kranz and O.D. Scherber, "Über einige kerroptische Bereichsbeobachtungen auf massivem Permalloy," Z. Angew. Phys. 28.Ed., Heft 1, 13-15 (1969).
6. L. Neel, "Effet des Cavites et des Inclusions sur le Champ Coercitif," Cashiers de Physique 25, 21-24 (1944).
7. L. Neel, "New theory of coercive force," Physica 15, 225-34 (1949).
8. D. Kuppers and J. Kranz, "Coercivity and domain structures of silicon-iron single crystal," J. Appl. Phys. 39, No. 2, 608-609 (1968).
9. R. M. Bozorth, Ferromagnetism, van Nostrand, New York (1951).
10. L. W. McKeehan, "Ferromagnetic anisotropy in nickel-cobalt-iron crystals at various temperatures," Phys. Rev. 51, 136-9 (1937).
11. J. D. Kleis, "Ferromagnetic anisotropy of nickel-iron crystals at various temperatures," Phys. Rev. 50, 1178-81 (1936).

Acoustic Emission Characterization of Failure
Mechanisms in Woven Roving Glass-Epoxy Composites

I. Roman* and K. Ono

Department of Materials Science and Engineering
School of Engineering and Applied Science

University of California, Los Angeles, CA 90024, USA

*Permanent address: Hebrew University, Jerusalem, Israel

ABSTRACT

Acoustic Emission (AE) behavior of woven roving glass-epoxy composites was investigated in order to characterize the various failure mechanisms operating during tensile loading. Both notched and unnotched samples were tested along five different directions: 0°, 15°, 25°, 35° and 45° with respect to one the fiber directions.

Resin pockets at cross-over points in the woven structure and transverse fiber-matrix interfaces failed at relatively low strains. The tensile fracture of fibers occurred at higher strains. The amplitude distribution of AE signals generated changed as the strain was increased. Initially, a single peak, centered around 34 dB (re. 1 μ V) was observed. Above 90% of the failure strain, high amplitude events became active at about 60 dB. For unnotched samples, many of the emissions up to the ultimate failure were of this amplitude and a double peak distribution resulted. The notched samples did not exhibit the double peak behavior.

Fractographic observations lead us to conclude that the lower amplitude emissions are characteristic of matrix cracking and/or interfacial separation and that the higher amplitude signals indicate fiber breakages. These results are in accord with reported results for other composite systems and can be employed to investigate more complex failure processes in glass-epoxy composites.

INTRODUCTION

A widespread deployment of advanced composites in high performance structures had led to a search for new material systems (i.e., reinforcement, matrix and their relative geometry) for specific applications. The structural efficiency of fabric reinforced composites is lower when compared with unidirectional laminates. However, lower fabrication costs and versatile properties have made them attractive for structural applications /1/. Successful utilization of such a composite material system, the understanding of the mechanics of which has not been fully established yet, requires reliable quality control procedures. Essential in the development of such procedures is the identification of correlations between relevant failure mechanisms and destructive and nondestructive testing parameters. Microstructural damage growth due to the loading of composite structures is complex and means capable of distinguishing between various failure modes must be established. Acoustic emission (AE) techniques, the amplitude distribution analysis in particular, are capable of characterizing different failure modes in a variety of composite material systems; e.g., Kevlar-epoxy /2/, glass-epoxy /3/ and carbon-epoxy /4/. Most of AE studies on composites have dealt with filament wound tanks and pipings or laminates of unidirectional laminae, while fabric reinforced systems have not received adequate attention. In the present study, mechanical and acoustic emission behaviors of woven roving glass-epoxy composites were

investigated. Our objective is to characterize various failure mechanisms operating during tensile loading of these woven laminates by means of their acoustic emission amplitude distributions.

EXPERIMENTAL

Specimens were prepared from commercially available sheets of woven roving glass-epoxy composites (Electroply, Grade GEE-101 per MIL-P-13949F/4B GFN). Each sheet consists of 13 plies of plain weave cloth with fiber weight fraction of 0.38. Straight sided tensile specimens with end tabs, 17.2 mm wide, 230 mm long, were cut from 2.36 mm thick plates with their sides either parallel to one of the fiber directions (0° samples) or at an angle to the fiber direction. The angles used for the different samples were 15° , 25° , 35° and 45° . Notched samples were 25 mm wide and had 90° notches on both sides to a depth of 3.9 mm, so that the ligament width (between the two notches) was 17.2 mm. An Instron (Model TT) with serrated-jaw wedge grips was employed at a constant cross-head speed of 0.02 mm/s in room air at ambient temperature.

AE characteristics evaluated during tensile testing were totalized AE event counts, rms voltages and the peak amplitude distribution of AE signals. A resonant type transducer (Model AC 175L, Acoustic Emission Technology Corporation [AET], Sacramento, California) and a preamplifier with 125-250 kHz filter (Model 160, AET) were used for all AE measurements. The transducer was acoustically coupled to the broad face of the tensile samples using a viscous resin. For the AE event count measurements and the amplitude distribution analysis, a microcomputer based AE instrumentation (Model 5000, AET) was employed. A true rms voltmeter (Model 3400A, Hewlett-Packard) was used for the rms voltage measurements.

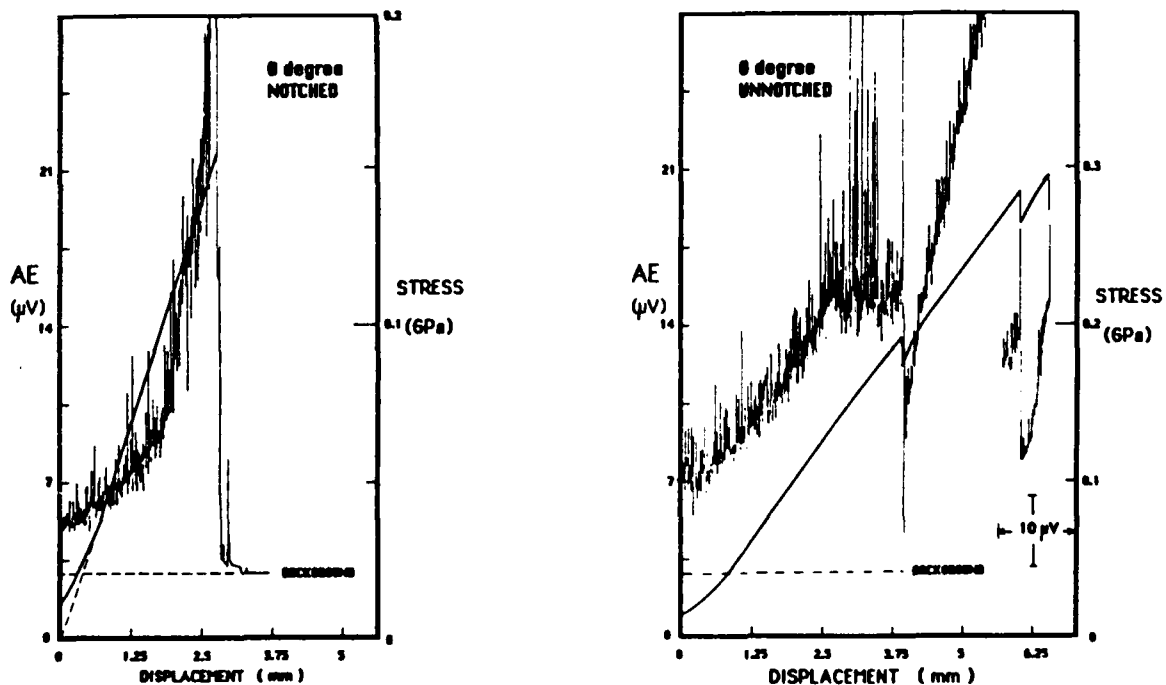


Fig. 1 Stress vs. time and rms voltage vs. time curves for notched and unnotched 0° samples. (Note different stress scales and change in rms voltage scale for unnotched sample.)

RESULTS AND DISCUSSION

Characteristic stress vs. time and rms voltage vs. time curves for both notched and unnotched 0° samples are shown in Fig. 1. The curves for all the samples loaded at an acute angle with respect to the fiber direction are qualitatively similar and are exemplified in Fig. 2. When 0° samples were loaded, it was observed that the stress increased linearly up to the failure of the samples. In all other cases, when inclined samples were loaded, a non-linear behavior followed the initial linear slope, much like the stress-strain curves of ductile alloys. The deviation from linearity reached a maximum for the 35° samples. For plain weave composites, this behavior was explained by employing the undulation model /1/. The model which utilizes the maximum strain criterion assumes that the first failures upon loading are transverse internal splits which occur at the center of the bundle undulation when the strain in this region exceeds the transverse bundle failure strain, ϵ_2^b . Subsequently, the failed areas propagate as the load (and hence the local strains) increases.

In all the unnotched samples several severe load drops were noticed during stressing. A total elongation for these samples was as high as 32 mm (for unnotched 35° samples of 113 mm gage length). Values of total elongation were much smaller (about 4 mm) for all the notched samples. The fracture stress for the unnotched samples decreased, as the fiber angle increased, from 301 MPa (0° samples) to 138 MPa (45° samples). This reduction was less in the notched samples, changing from 157 MPa (0° samples) to 96 MPa (45° samples). These values also indicate notch sensitivity in all the experimental conditions studied. All the samples failed without exhibiting a "knee" in the stress-strain curve, which is characteristic of transverse cracking in cross-ply laminates. This is in accord with Harris et al. /5/ and in contrast to McGarry and Desai /6/ who observed a "knee" in both woven and non-woven laminates.

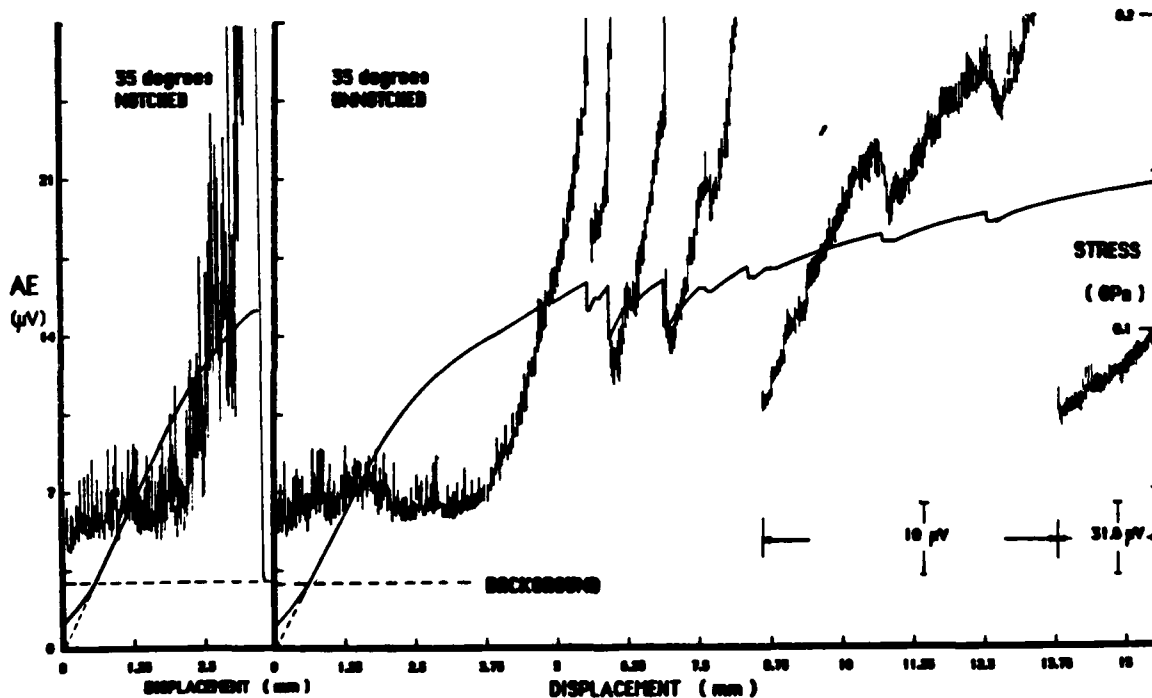


Fig. 2 Stress vs. time and rms voltage vs. time for notched and unnotched 35° samples. (Note change in rms voltage scale for unnotched sample, and the fact that only part of the record is shown.)

Both the rms voltage level and the total AE event counts for all the samples increased with the tensile strain, gradually in the beginning and very steeply as the failure strain was approached. All rms voltage curves were modulated by numerous burst emission spikes, the number and intensity of which increased with the strain level.

In spite of these qualitative similarities in the AE behavior of the different experimental conditions studied, some differences were noticed. First, as can be seen from Figs. 1 and 2, distinct differences in the AE behavior parallels the different mechanical behavior of notched and unnotched samples. The rms voltage level of all the notched samples initially increased gradually up to about 8 μ V. At about 80% of the failure strain, a sharp increase in the rms voltage level was noted which exceeded 32 μ V. before the ultimate failure. The total event counts for all the notched samples were in the range of $45,000 \pm 6,000$ and the AE instrumentation was capable of processing about 70% of these events, that is, only $31,000 \pm 9,000$ events were analyzed by the AE microcomputer based system, as to their characteristics, such as peak amplitude.

When comparing this behavior to that of the unnotched samples, the AE activity of the unnotched samples was clearly more pronounced. total event counts detected increased from 167,400 (0° unnotched sample) to over 503,000 (45°, unnotched sample). Because of the high activities, the AE instrumentation processed less than half of these events. The rms voltage level of the unnotched and inclined samples (which is exemplified in Fig. 2, raised to a level of about 6 μ V. immediately upon loading and remained at this level well into the non-linear region (of the stress vs. displacement curve). At this point the rms voltage level increased sharply as a result of some increases in the peak amplitude but mainly due to drastic increase in event rate. This increase in event rate made it impossible for the AE instrumentation to distinguish between different events thus resulting in a decrease in the AE count rate. The maximum rms voltage reached at failure increased from levels exceeding 50 μ V. (15° unnotched samples) to 160 μ V. (45° unnotched samples).

The differences in the AE activity were also manifested in the peak amplitude distribution for notched and unnotched samples. For example, the distribution for the whole test of the notched 35° sample exhibited a major peak (about 2900 events) around 34 dB (re. 1 μ V) and a high amplitude trail elevated to a level of about 700 events starting at around 48 dB, (Fig. 3a.) In contrast, two peaks having essentially identical heights of 10,000 to 15,000 events were observed in the distribution for the unnotched 35° sample, Fig. 3b. The first coincided with the 34 dB peak and the second was centered around 60 dB. The height of the first peak for all notched samples was in the range of 2000 to

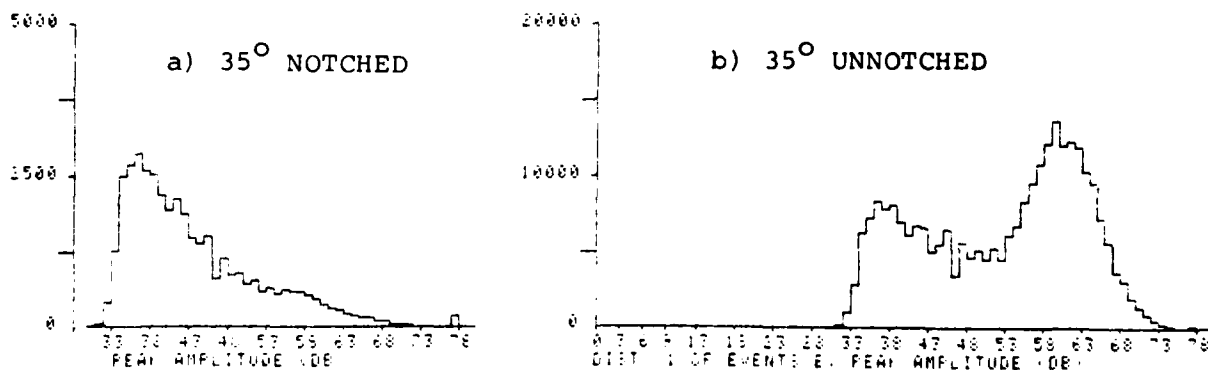


Fig. 3 AE peak amplitude distribution for the entire loading period of 35° samples.

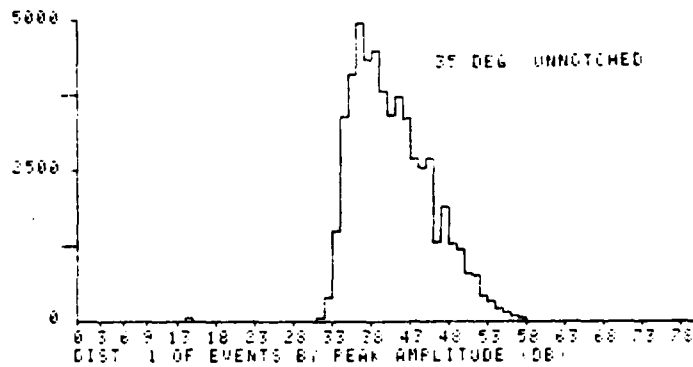


Fig. 4 AE peak amplitude distribution for an unnotched 35° sample loaded up to 0.4 ϵ_f .

3000 events. However, the height of the high amplitude tail increased from 80 events for the 0° sample to about 700 events for the 35° sample.

In order to ascertain the origin of these differences, the AE peak amplitude distribution was determined, using both notched and unnotched samples, as a function of tensile strain. It was found that, up to about 90 % of the failure strain, the peak amplitude distribution for most samples exhibits a single peak centered around 34 dB (e.g., Fig. 4). Above this strain level, higher amplitude AE events became noticeable. These higher amplitude events occurred over a longer period of time and increased in amplitude from 48 to 60 dB as stressing progressed in the case of the unnotched samples. In the final peak amplitude distribution this produced two strong peaks for the unnotched samples. For the notched samples, however, the number of high amplitude emissions was limited and only produced an elevated tail at high amplitudes.

The fracture surfaces produced during tensile loading were examined visually and in the scanning electron microscope (SEM). The macroscopic crack profiles of all the experimental conditions tested are shown in Fig. 5. A gradual discoloration was noted in the failed unnotched samples which reached a maximum for the 35° unnotched samples. This appearance is indicative of significant damage throughout the entire gage section, which explains the difference of about one order of magnitude in the total event counts between unnotched and notched samples. For the latter, damage is mostly localized in the fractured plane and no significant discoloration was observed. In order to verify whether the damage in the discolored regions is limited to matrix



Fig. 5 Macroscopic crack profile of all experimental conditions tested.

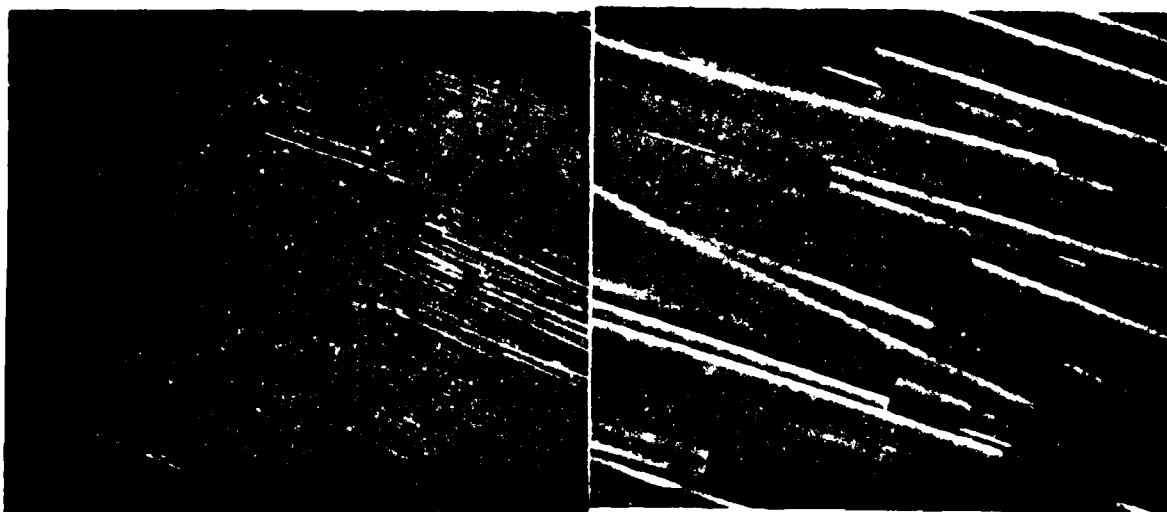


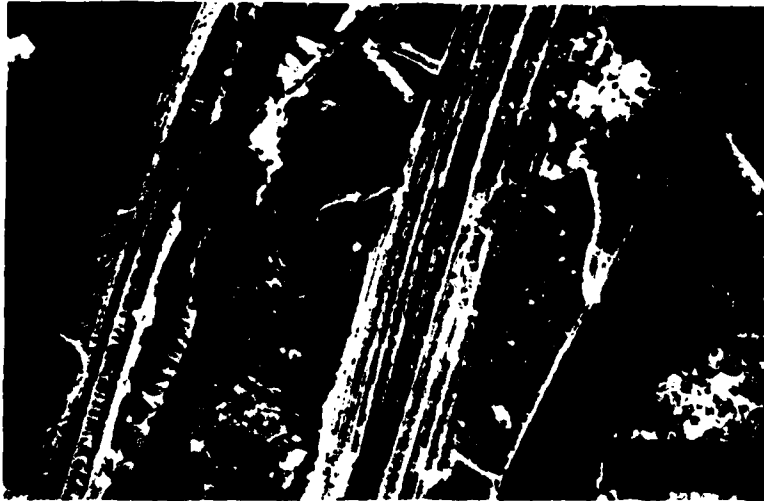
Fig. 6 SEM micrographs showing broken fibers in the woven glass roving in a region remote from the main fracture surface of a 35° unnotched sample.

cracking and delamination or includes also fiber breakage, the matrix of a sample from this area was burnt off. The remaining woven glass roving were examined optically and in the SEM. Another sample was loaded to a point where the higher amplitude emissions just started to become noticeable. Burning off the matrix and examining the remaining woven glass roving, we found a few broken fibers, the number of which was comparable to a virgin sample. On the other hand, Figure 6 contains typical micrographs which were taken from the fractured sample. These clearly demonstrate the fact that fiber breakage took place. These observations show that fiber fractures accompany the high amplitude emissions and that only matrix cracking and fiber-matrix debonding are responsible for the low amplitude emissions. It is interesting to note that both fill and warp fibers have cracked in Fig. 6. This finding might explain the increase in AE activity with testing angle for the unnotched samples. As the angle increases the probability of fiber failure increases since both warp and fill fibers are loaded.

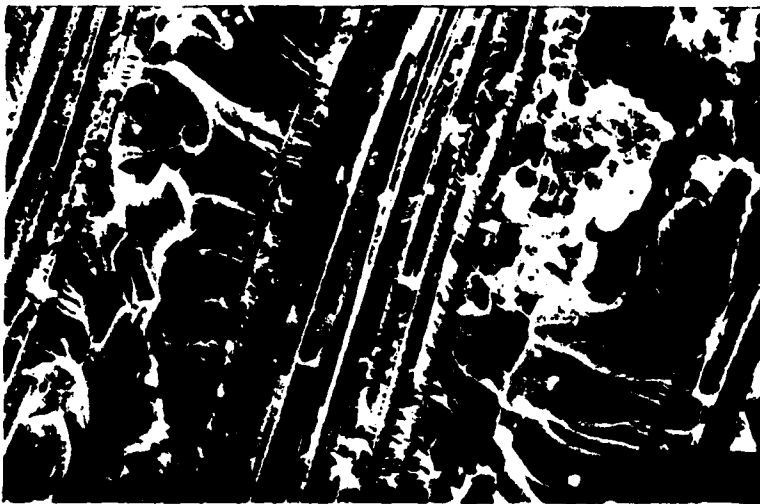
Figure 7 contains SEM fractographs typical of the fracture surfaces of the notched 0° and 35° samples. In both cases the fracture surfaces have a brittle appearance at low magnification consisting of damaged transverse bundles, brittle matrix fracture and few short pullouts. The crack traverses resin pockets at cross-over points in the woven structure, transverse fiber-matrix interfaces (both within bundles and at bundle-matrix boundaries), and longitudinal fiber bundles. In the case of the 35° samples, the transverse fiber bundles contain numerous cracks, which are probably due to the fact that in the inclined geometry both longitudinal and transverse fibers experience tensile stresses. Thus, it is reasonable to assume that these additional transverse fibers fractures in the inclined samples are responsible for the higher intensity of the second peak in the amplitude distribution for this loading geometry.

The observed AE and mechanical behavior of the composites in the different experimental conditions utilized in this study can be explained by considering the following sequence of events that occur upon loading:

When the woven roving glass epoxy composites which contain bundles of crimped fibers are stressed, the tensile component attempts to straighten out the undulation in the stressed bundles. If load is applied at an acute angle to the fiber direction, the tensile stress also causes fiber rotation so that the



0° NOTCHED



35° NOTCHED

Fig. 7 Typical SEM fractographs showing the fracture surfaces of notched 0° and 35° samples.

angle between (both the fill and warp) fibers and the loading direction decreases. Each of these two phenomena imposes high local compressive stresses on the resin pockets which ultimately cause matrix cracking. In addition, friction is induced between the rotating fibers and matrix. The friction eventually can damage the fibers and increases with loading angle and stress level. Another failure mode that is operative at low strains is in the form of transverse internal splits which occur at the center of the bundles undulation as discussed earlier. These mechanisms persist throughout the entire loading period. However, when local strains build up sufficiently, fiber fractures commence in increasing numbers, leading to the ultimate failure of the samples.

In the unnotched samples, considerable matrix damage along the entire gage length precedes the final stage of fiber fracture which occurs at relatively high macrostrains of up to 25%. This level of tensile strain is mostly due to fiber rotation, straightening out of crimped bundles and matrix cracking. Thus, fiber microstrains build up over the entire gage section after the sample has undergone considerable elongation. Conversely, the microstrains in the notched samples are elevated rapidly ahead of the notches due to the significant strain concentration effect of the notches. This causes low tensile elongation resulting in little matrix damage before the fibers (and hence the sample) fail, and the entire damaged zone is localized between the notches. This sequence of events explains the vast differences in ductility between the notched and

unnotched samples. The differences in the damage zone size, i.e., the entire gage length for unnotched samples vs. localized region between the notches for notched samples, account for the large differences in the total event counts.

The present findings pose a potentially serious limitation in applying AE techniques to the integrity monitoring of woven composite structures. When a strength-impairing notch exists, the expected number of AE events is drastically reduced. The amplitude distribution also lacks a high amplitude peak, often considered as a measure of progressive fiber damages. Extra precaution in the interpretation of AE results is therefore advised when notches are present in a structure.

Consequently, the higher amplitude emissions indicate fiber breakages whereas the lower amplitude signals are characteristic of matrix cracking and/or interfacial separation. This conclusion is in line with the theoretical prediction /1/ that resin pockets and transverse fiber-matrix interfaces fail at relatively low strains followed by longitudinal fibers fracture at higher strains.

CONCLUSIONS

1. Higher amplitude emissions detected during tensile loading of woven glass epoxy composites in the range of 48 to 60 dB (re. 1 μ V) are characteristic of fiber breakage.
2. Lower amplitude signals (around 34 dB) indicate matrix cracking and/or interfacial separation.
3. The presence of notches drastically alters the number of AE events and the peak amplitude distribution.

ACKNOWLEDGEMENTS

This work was supported by the Office of Naval Research, Physics Program.

REFERENCES

1. T. Ishikawa and T.W. Chou, in Progress in Science and Engineering of Composites, ICCM-IV, Vol. 1, Tokyo, 1982, pp. 489-496.
2. I. Roman, A. Mittelman, M. Davidovitz and G. Marom, Session 2, pp. 1-2, in Proceedings of the 1st Inter. Symp. on Acoustic Emission From Reinforced Composites, SPI, San Francisco, July 17-21, 1983.
3. G.D. Sims, G.D. Dean, B.E. Read and B.C. Western, J. of Materials Science, 12 (1977) 232-234.
4. D. Valentin, Ph. Bonnian and A.R. Bunsell, Composites, 14[4] (1983) 345-351.
5. B. Harris, F.J. Guild and C.R. Grown, J. of Physics D: Applied Physics, 12 (1979) 1385-1407.
6. F.J. McGarry and M.B. Desai, Proc. 19th Conf. of SPI, Paper 16-E, 1959.

**Fracture Induced Acoustic Emission of A533B Steel - Effects of
Test Temperature and Fracture Mechanisms**

H.B. Teoh, K. Ono and I. Roman*

**Department of Materials Science and Engineering
School of Engineering and Applied Science
University of California, Los Angeles, CA 90024 USA
*Permanent address: Hebrew University, Jerusalem, Israel**

ABSTRACT

AE behavior of A533B steel was investigated during fracture tests as a function of test temperature. Pre-cracked and as-notched Charpy slow bend tests were used. Tests were also interrupted and fractographic information was obtained. Various AE parameters were determined using a microcomputer-based AE instrumentation and related to mechanical and topological data. In addition, orientation dependence and effects of heat treatment were studied. The temperature-dependence of AE events was vastly different between the LT and ST orientations. On the other hand, pre-cracked and as-notched samples had similar temperature dependences, but with different levels of AE events.

These findings were interpreted in terms of several fracture mechanisms and will be discussed in detail. It is noteworthy that AE due to ductile crack growth is buried among those from inclusion decohesion.

INTRODUCTION

Previous studies have indicated that low alloy steels exhibit anisotropic acoustic emission (AE) behavior during deformation and fracture /1,2/. Such AE behavior has been attributed to the presence of nonmetallic inclusions. During fracture tests, short-transverse (ST in terms of the ASTM designation) orientation samples emitted burst-type AE signals which persisted from the elastic region to maximum load. The AE source has been established to be the decohesion of elongated MnS inclusions. On the other hand, longitudinal (LT) orientation samples exhibited a much lower AE activity. The AE activity was most prominent only at general yield, and is due to plastic deformation and certain ductile fracture mechanisms.

To extend further the understanding of the fracture-induced AE behavior of A533B steel, three-point bend tests were performed in this study as a function of test temperature. The results indicated that ST samples generated larger event counts than LT samples at all temperatures. In addition, test temperatures have minor effects on the event counts of both LT and ST samples except at low temperatures when ST samples produced less events than at high temperatures. Occurrence of cleavage fracture can be identified by the appearance of large-amplitude AE events.

Fractographic analysis shows that A533B steel undergoes different deformation and fracture processes during fracture testing, depending on the heat-treatment and specimen orientation. AE measurements during such a test reveal AE signals with a variety of peak amplitude distribution characteristics.

In order to correlate fracture mechanisms and the AE signals they emit, we performed slow-bend tests on quenched (Q) and quenched and tempered (QT) samples. To isolate the fracture processes, interrupted tests were conducted whereby samples were loaded to selected load levels, unloaded and fractured by impact (at -196°C) to reveal the fracture surfaces. From AE measurements and

post-test fractographic analysis, the AE signals associated with each fracture mechanism were then identified. The results showed that tear and shear fracture processes as well as microvoid coalescence emitted low-amplitude AE events, with peak amplitude values similar to those from plastic deformation. Quasi-cleavage and cleavage processes emitted high-amplitude events, in agreement with results reported in the literature.

Decohesion of MnS inclusions has been shown to generate AE events with a broad range of amplitudes, with their peak amplitude distributions having the characteristic Weibull distribution. When decohesion occurs, AE events from this process would overwhelm those from plastic deformation or from such fracture processes as tear, shear or microvoid coalescence; only cleavage or quasi-cleavage fracture can be separated on the basis of peak amplitude.

MATERIAL AND EXPERIMENTAL PROCEDURES

The material used in this study is a low-alloy ASTM A533B Class 1 steel plate of 165 mm thickness. The chemical composition (wt.%) consists of 0.18C, 0.25 Si, 1.43 Mn, 0.013 P, 0.005 S, 0.50 Mo, 0.66 Ni, 0.28 Cr, 0.01 Cu, Fe (balance). Standard Charpy V-notch samples (10 x 10 x 55 mm) were used. Details about test procedures can be found elsewhere /2/. Two specimen orientations were selected: LT and ST. The specimens were given one of three heat-treatments: Q (930°C, 1 hr, oil-quenched), QT (930°C, 1 hr, oil-quenched + 650°C, 24 hr, oil-quenched) or NT (930°C, 1 hr, air-cooled + 650°C, 24 hr, furnace-cooled). Some of the specimens were fatigued on an ETI rotary bending machine to introduce precracks of 1 mm. For tests above room temperature, the specimens were heated by incandescent light bulbs; for tests below room temperature, they were immersed in n-propyl alcohol which was cooled by liquid nitrogen.

The AE parameters evaluated were cumulative AE event counts, rms voltage and peak amplitude distribution of AE signals. AE measurements were obtained using a 175-kHz resonant transducer (AET Corporation AC 175L) and a preamplifier (60 dB gain) with 125-250 kHz filter. The transducer was coupled to specimen using a stainless steel waveguide. A true rms voltmeter provided the rms voltage data. AE event counts measurements and peak amplitude distribution analysis were obtained from a microcomputer-based AE instrumentation (AET Corporation Model 5000) and an amplitude distribution analyzer (AET Corporation Model 203). The input noise level was 1.4 μ V. The threshold value for both Model 5000 and Model 203 was 15 μ V.

RESULTS AND DISCUSSION

Room temperature tests of ST-orientation samples in the normalized and tempered conditions (hereafter referred to as NT/ST samples) with precracks showed active AE behavior beginning at the precrack load of 4.4 kN and persisting to maximum load. AE signals mainly consist of burst emissions which are represented by numerous rms voltage spikes and are due to the debonding of MnS inclusions. NT/LT samples exhibited a completely different AE behavior. Most of the AE activity was of the continuous type and was confined to the vicinity of general yield, where the rms voltage curve showed a peak. The rms voltage curve also contained numerous spikes, especially after maximum load. The AE behaviors of these NT samples are similar to those of the corresponding as-received samples /2/.

Testing of NT/ST samples at temperatures between -75° and 150°C yielded AE behaviors which are generally similar to the room temperature behavior of the samples of corresponding orientation. However, one important feature at low

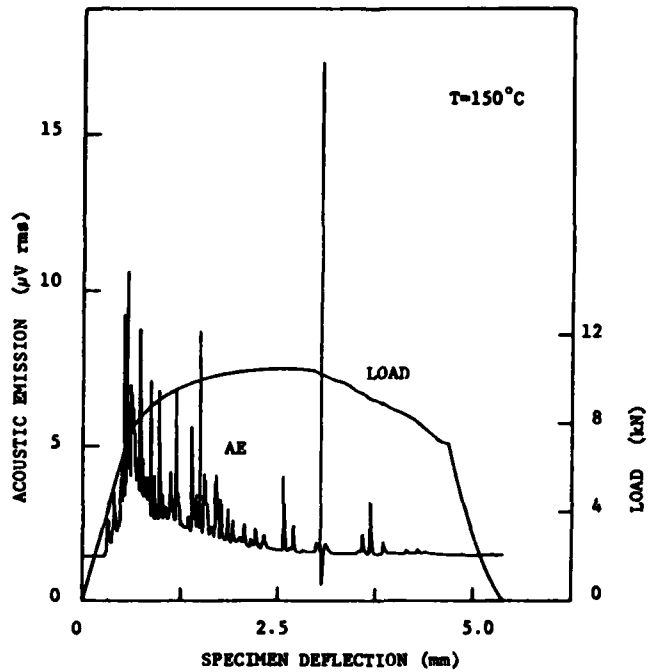
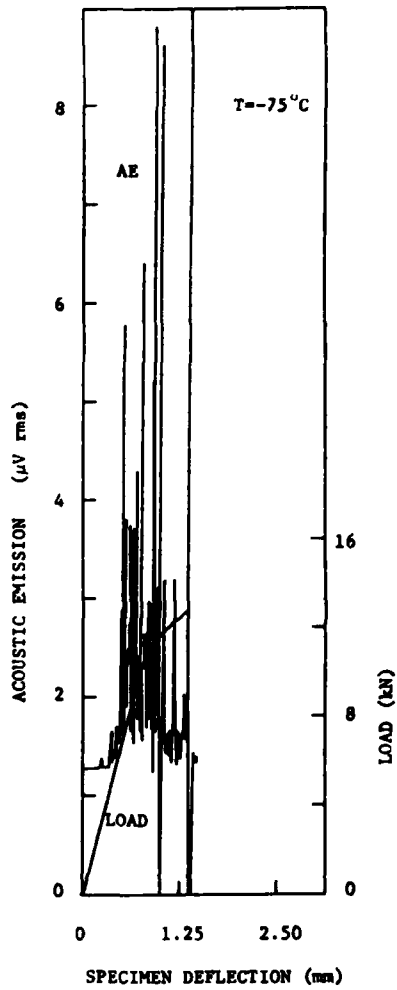


Fig. 1 Load and AE data for precracked NI/ST samples tested at a) -75°C and b) 150°C .

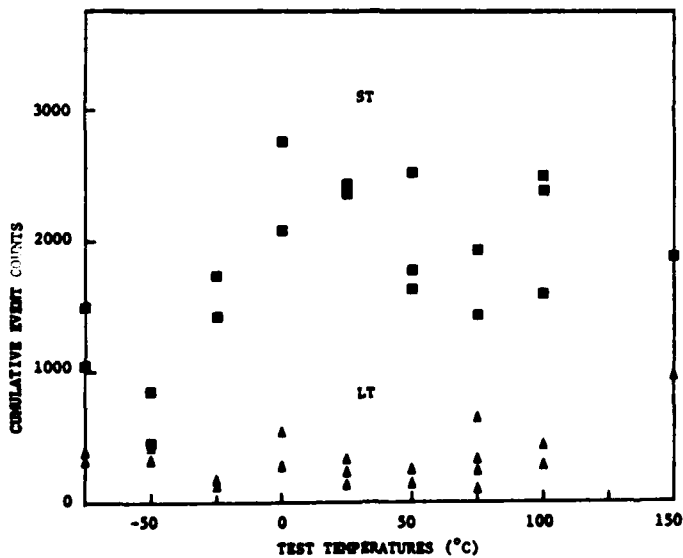


Fig. 2 Cumulative event counts vs. test temperatures for pre-cracked NI/LT and NI/ST samples.

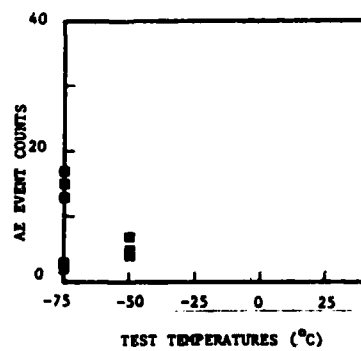


Fig. 3 Large amplitude ($> 1 \text{ mV}$) events vs. test temperature.

temperatures should be noted. When tested at -50° or -75°C , the precracked samples fractured by cleavage at load levels near general yielding, while a few samples failed after some plastic deformation. The AE and load data for tests at -75°C and 150°C are shown in Fig. 1.

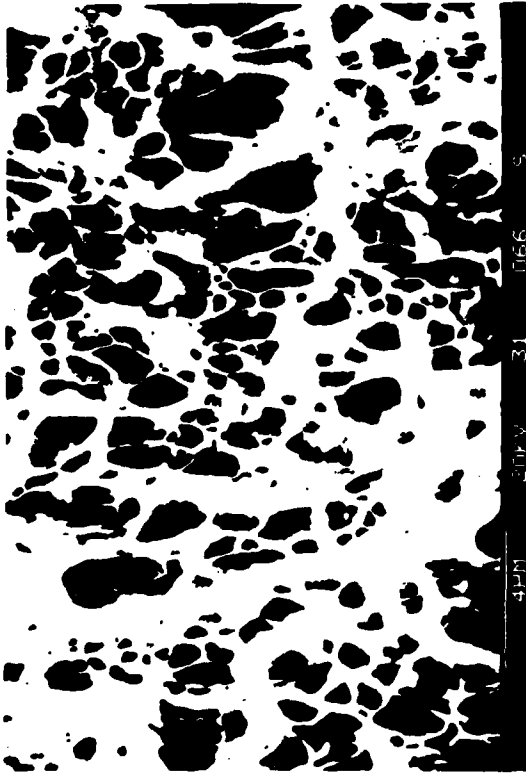
Figure 2 shows the effects of test temperature on the cumulative event counts of precracked LT and ST samples. For NI/ST samples, their event counts between -25° and 150°C lie within a scatter band between 1400 and 2700 events. This implies that the source of burst emissions in these samples, namely, MnS inclusion decohesion, is temperature independent at or above -25°C and agrees with the concept that the inclusion decohesion process is stress-controlled /2/. As long as stresses acting on MnS inclusion surfaces exceed the critical stress for debonding, the inclusion would separate from the matrix, regardless of test temperature, producing a burst emission. At -50° and -75°C , the event counts have values between 500 and 1500 events. Since the event counts at these low temperatures were accumulated to the point of specimen failure only, the truncated specimen deflection probably accounted for the reduced number of events. In addition, cleavage-induced AE source that operates at these temperatures did not generate as many emissions as inclusion decohesion.

NI/LT precracked samples showed an essentially temperature independent behavior in terms of AE events. Except for the data at 150°C , all the event counts data fall within a scatter band between 100 and 650 events. It is obvious that the LT samples generated much lower event counts than their ST counterparts at the same test temperature. In fact, for the entire range of test temperatures (except for the test at 150°C), ST-samples always produced higher event counts than LT samples.

AE signals due to cleavage have high peak amplitudes, typically greater than 1 mV /3,4/. From the amplitude distribution of AE signals, we can estimate the events due to cleavage as those with peak amplitudes exceeding 1 mV. The results in Fig. 3 indicate the large-amplitude emissions contributed no more than 20 events per test and that they were not detected for samples tested above -25°C . The number of events is reasonable since immediately after cleavage cracks have been nucleated in front of the crack tip, not much crack propagation is required before final failure of the sample occurs. The cleavage crack will extend in an unstable manner if the local tensile stress at the crack tip exceeds the critical value for unstable cleavage /5/. Nevertheless, despite their small numbers, the large emissions are clearly identifiable on the amplitude distribution plots. They also caused the slope of the distributions to decrease.

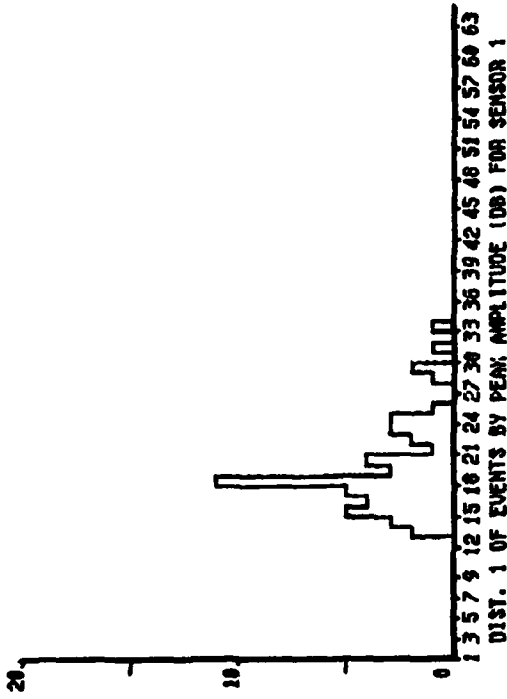
Figures 4 to 9 show the fractographs of the various fracture mechanisms found in A533B steel and the peak amplitude distributions of the associated AE signals. Figure 4 reveals the fracture surface of a QT/LT sample which is characterized by a fibrous fracture zone in the form of a thumbnail in the center of the sample. The thumbnail crack grew in the center of the sample where maximum constraint existed. Large troughs, indicative of previous sites occupied by inclusions, were distributed generously within the fibrous zone. They were aligned perpendicular to the crack front and some reached lengths of 400 μm . The rest of the surface in the fibrous zone was covered by finer dimples of about 1 to 2 μm diameter which were formed by microvoid coalescence.

The AE associated with dimple fracture consists of low amplitude emissions as evident in the amplitude distribution also shown in Fig. 4. The emissions have peak amplitudes between 27 and 47 dB, with a majority with amplitudes below 39 dB. Here, 0 dB refers to 1 μV at the transducer. Note that the amplitude scale used in Figs. 4 - 9 refers to 0 dB at 5 μV that requires the addition of 14 dB in order to convert to the more commonly used scale. This range of peak amplitude is similar to that due to plastic deformation.



40PM 20KV X31 0266 S

Fig. 4 Fracture surface and the peak amplitude distribution for fibrous fracture zone of a QT/LT sample.



40PM 20KV X31 0288 S

Fig. 5 Fracture surface and the peak amplitude distribution for a QT/ST sample showing MnS inclusions and inclusion-induced troughs.

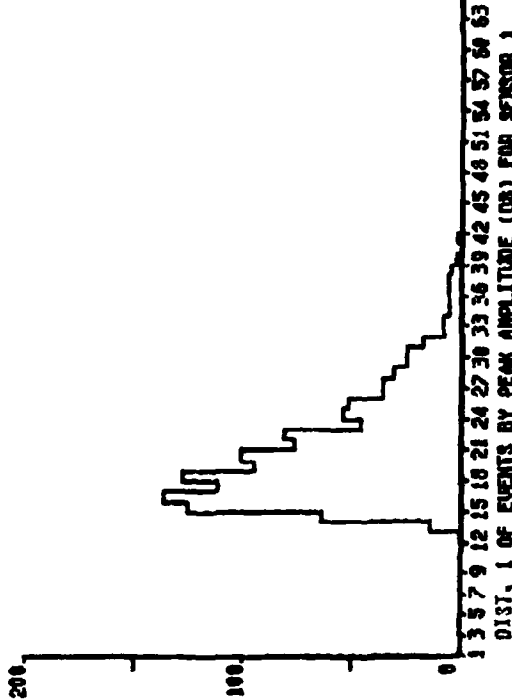




Fig. 6 Fracture surface and peak amplitude distribution for a Q/LT sample showing tearing at the notch-root. Fragments of machined surfaces are also shown.

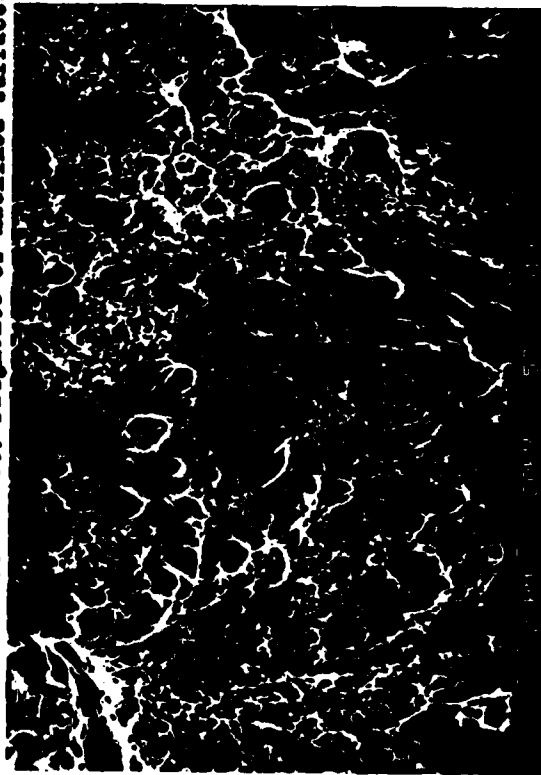
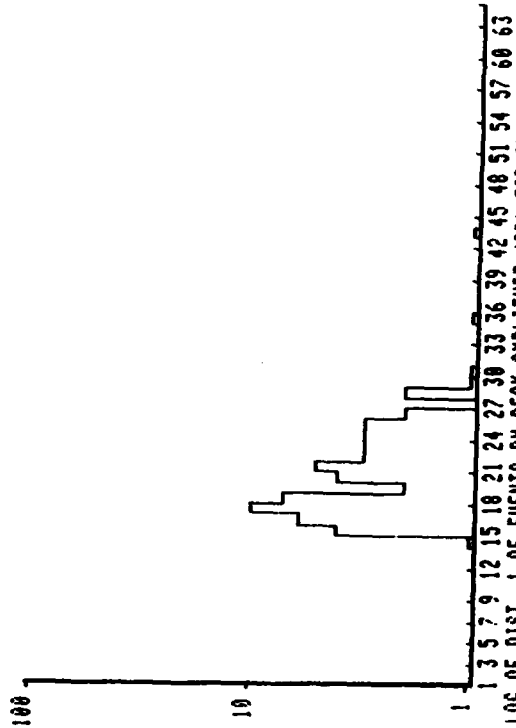


Fig. 7 Fracture surface and peak amplitude distribution for Q/LT sample showing shear dimples.

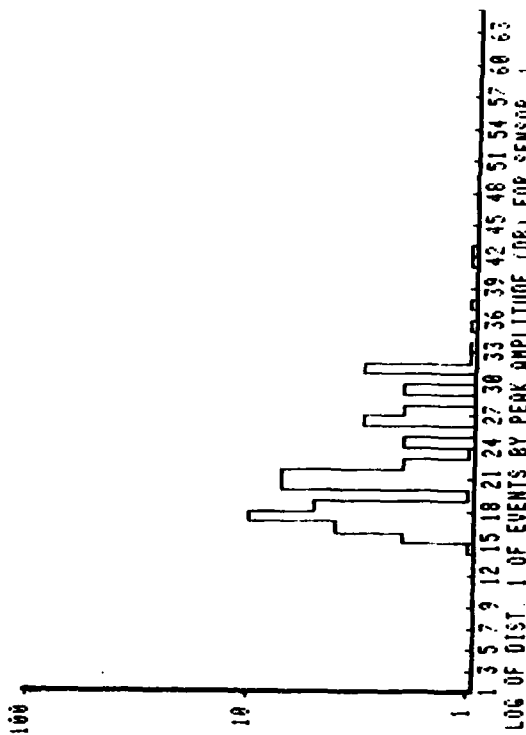




Fig. 8 Fracture surface and peak amplitude distribution for quasi-cleavage fracture of Q/LT sample.

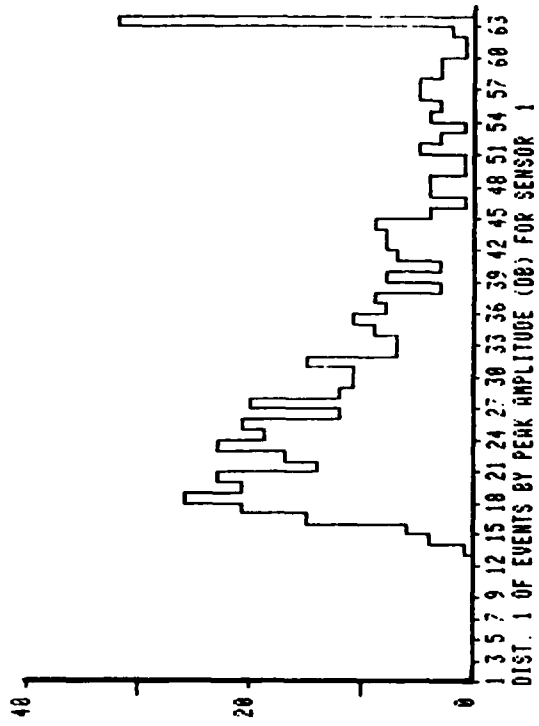


Fig. 9 Fracture surface and cumulative peak amplitude distribution for cleavage fracture at -75°C of pre-cracked NT/ST sample.

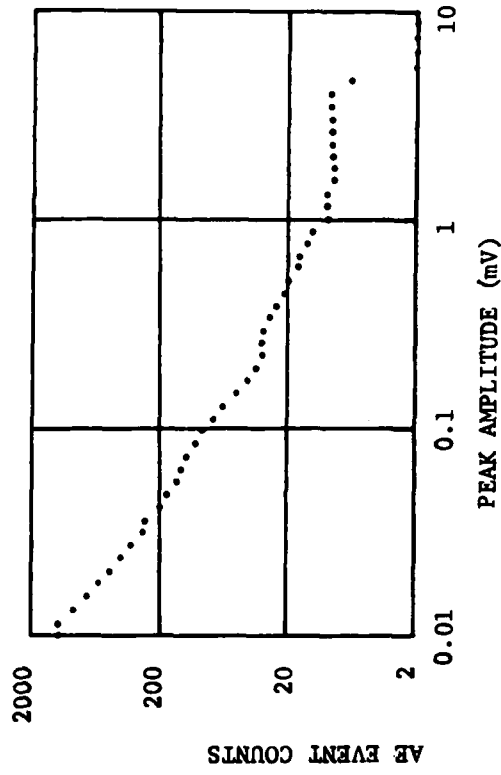


Figure 5 shows the fracture surface and peak amplitude distribution of a QT/ST sample. Like the QT/LT sample discussed above, the fracture surface of the QT/ST sample is characterized by a fibrous zone in the form of a thumbnail in the center of sample. The fibrous zone is covered almost entirely by large inclusion-induced troughs, however, and some of them were 1 mm long. Some of the inclusions have been identified to be MnS and are visible in Fig. 5. The QT/ST as well as NT/ST samples generated burst emissions which are associated with the decohesion of MnS inclusion. Their AE behaviors are active and are represented by numerous spikes on the AE rms voltage curve which begins as soon as the loading of sample commences. The AE activity reaches a peak at the general yield and persists to maximum load. The emissions have peak amplitudes between 27 and 54 dB, as indicated in Fig. 5; a majority of the emissions have peak amplitudes below 36 dB. Their cumulative peak amplitude distributions show the characteristic Weibull distribution with the exponent between 0.3 and 0.4 /2,6/.

The fractograph in Fig. 6 shows clearly the nature of crack propagation from the notch root of a Q/LT sample with no precrack. The lower part of the fractograph reveals the highly distorted surface of the machined notch, where long elongated dimples had initiated at multiple sites. The cusps of these severely distorted dimples point towards the notch. Examination of the matching half of the sample reveals similarly pointed dimples, suggesting that they were formed by a tearing mechanism. The dimples formed an extensive stretch zone between 30 and 50 μ m wide, running across the entire specimen width. The stretch zone is followed by a region containing large shear dimples which are separated by finer, round dimples (Fig. 7).

The tear and shear processes, which occurred before or during general yielding of sample, generated low-level AE consisting primarily of low-intensity continuous-type emissions. These emissions have peak amplitudes ranging from 29 to 45 dB with most events between 30 and 40 dB, as shown in Figs. 6 and 7.

Figure 8 shows quasi-cleavage colonies which occurred near the notch root, but beyond the shear dimples of Fig. 7. The cleavage facets are found in samples that were loaded to near or beyond the maximum load. These emitted high amplitude AE signals with peak amplitudes exceeding 100 μ V. Since these large emissions were absent in samples that did not contain cleavage facets, cleavage fracture near maximum load must have generated the high amplitude emissions. This agrees with observations reported in the literature /3,4/. The high-intensity voltage spikes caused a large increase in the number of events. This becomes apparent when the amplitude distributions in Figs. 7 and 8 are compared. The largest increase in event counts occurred during the falling load period, when macrocrack propagated in the sample. The macroscopic fracture contributed about 80 to 85% of the total event counts. Some of these events have very large amplitudes as indicated by their peak amplitude distribution in Fig. 8. Although events with peak amplitude below 42 dB still dominated, there were also many events with higher amplitudes, including some which saturated at 77 dB. The appearance of the large amplitude events caused the slope of the cumulative amplitude distribution to decrease.

Figure 9 shows the cleavage fracture surface of an NT/ST sample tested at -75° C. The sample failed during test at a load slightly above general yield. The surface contains cleavage facets with some ductile tearing. Secondary cracks are also observed. The amplitude distribution for this sample, Fig. 9, indicates the presence of events with peak amplitude up to 74 dB. Note that Fig. 9 shows the cumulative peak amplitude distribution of the AE signals. Events with peak amplitudes above 1 mV (60 dB) differentiate this distribution from the Weibull distribution characteristic for MnS inclusion decohesion. The cleavage fracture of NT samples accounted for about 15 to 70% of the total event counts. Like the Q samples, this was again indicated by a jump in the total event counts during the falling load period.

From AE measurements and fractographic analysis, the ranges of the peak amplitude of AE events from various fracture mechanisms were identified. The results indicate that tear/shear or dimple fracture generated AE with peak amplitudes comparable in values to those from plastic deformation. When inclusion decohesion occurs, the events from this process would obscure those from other processes except for events from cleavage fracture.

CONCLUSIONS

1. Test temperature has little effects except at 150°C on the event counts of precracked NT/LT samples.
2. The event counts of precracked NT/ST samples were almost independent of temperatures above -25°C, indicating that MaS decohesion process is temperature independent.
3. Tear and shear types of ductile cracks and microvoid coalescence generated only low-amplitude AE events with peak amplitudes below 47 dB (ref. 0 dB at 1 μ V).
4. Quasi-cleavage and cleavage processes emitted large-amplitude AE events, some of which had peak amplitudes between 54 and 77 dB.
5. When inclusion decohesion occurred, AE events from the decohesion completely buried and obscured those due to tearing, shear cracking and dimple fractures.

REFERENCES

1. K. Ono, G. Huang and H. Hatano, Proc. 8th World Conf. on Nondestructive Testing, Cannes, France, September 1976, Conference Secretariat, Paris, 1976, Section 3K, Paper 3K3, pp. 1-10.
2. K. Ono and M. Yamamoto, Mat. Sci. Engr., 47 (1981) 247-263.
3. N.W. Ringshall, K. Okamoto, T. Nakamura and J.F. Knott, Proc. 5th Int. AE Symposium, Tokyo, Japan, November 1980, pp. 429-442.
4. M.A. Khan, T. Shoji and H. Takahashi, Metal Science, 16 (1982) 118-126.
5. R.O. Ritchie, J.F. Knott and J.R. Rice, J. Mech. Phys. Solids, 221 (1973) 394-410.
6. K. Okajima and K. Ono, Proc. 5th Int. AE Symposium, Tokyo, Japan, November 1980, pp. 270-281.

END

FILMED

10-84

DTIC